Photoacoustics 41 (2025) 100675

Contents lists available at ScienceDirect

Photoacoustics

journal homepage: www.elsevier.com/locate/pacs

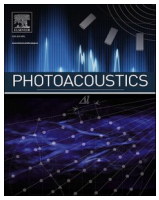

Classification and risk assessment of ovarian-adnexal lesions using parametric and radiomic analysis of co-registered ultrasound-photoacoustic tomographic images

Yixiao Lin [a], Quing Zhu [a,b,*]

[a] Biomedical Engineering Department, Washington University in St Louis, United States
[b] Radiology Department, School of Medicine, Washington University in St Louis, United States

ARTICLE INFO

Keywords:
Ovarian-adnexal lesions
O-RADS
Co-registered ultrasound-photoacoustic tomography
Multiparametric ultrasound
Radiomics

ABSTRACT

Ovarian-adnexal lesions are conventionally assessed with ultrasound (US) under the guidance of the Ovarian-Adnexal Reporting and Data System (O-RADS). However, the low specificity of O-RADS results in many unnecessary surgeries. Here, we use co-registered US and photoacoustic tomography (PAT) to improve the diagnostic accuracy of O-RADS. Physics-based parametric algorithms for US and PAT were developed to estimate the acoustic and photoacoustic properties of 93 ovarian lesions. Additionally, statistics-based radiomic algorithms were applied to quantify differences in the lesion texture on US-PAT images. A machine learning model (US-PAT KNN model) was developed based on an optimized subset of eight US and PAT imaging features to classify a lesion as either cancer, one of four subtypes of benign lesions, or a normal ovary. The model achieved an area under the receiver operating characteristic curve (AUC) of 0.969 and a balanced six-class classification accuracy of 86.0 %.

1. Introduction

Transvaginal ultrasound (US) is widely used for initial evaluation of ovarian-adnexal lesions. The Ovarian-Adnexal Reporting and Data System (O-RADS) provides a consensus guideline for stratifying the malignancy risk of ovarian-adnexal lesions based on grayscale and Doppler US [1,2]. However, despite its high sensitivity in detecting cancer, O-RADS is challenged to accurately diagnose lesions with atypical appearances, resulting in a low specificity. Consequently, while over 40 % of patients with adnexal lesions undergo surgeries, less than 10 % of the excised lesions are malignant, suggesting that many patients could have more conservative management [3]. MRI provides superior specificity and a higher positive predictive value (PPV) because it can more accurately distinguish the type of fluid and solid components inside a lesion [4,5]. Contrast-enhanced US (CEUS) has also been shown to moderately improve the diagnostic specificity [6,7]. However, both CEUS and MRI involve contrast agents and require more complicated examination procedures.

Photoacoustic tomography (PAT) uses hemoglobin as an endogenous contrast agent to image vasculature. Compared to Doppler US, PA imaging can detect smaller vessels and reflect a lesion's vascularity more accurately because it does not depend on either blood flow or the US probe's orientation during imaging [8,9]. PA can be readily integrated with US systems for various clinical applications [10–12]. Earlier publications from our group have shown that when assessing the cancer risk of an ovarian-adnexal lesion, incorporating PAT total hemoglobin concentration and blood oxygenation saturation information improved diagnostic accuracy [12,13]. However, our earlier approaches did not explore the use of quantitative US and PA parameters, radiomic features, and machine-learning models for accurate diagnosis of complex ovarian lesions.

Parametric US extracts parameters of tissue's response to US from radiofrequency (RF) data. These parameters are intrinsic tissue properties that are operator-independent and do not require capturing the entire lesion on a single US scan. Studies have demonstrated the clinical efficacy of these algorithms in imaging various organs and tissue types [14–16]. Similar parametric algorithms are also applicable to PA imaging.

Radiomics is a statistical approach to image analysis that has been applied to various modalities in a range of oncological applications [17–19]. Both parametric algorithms and radiomics computationally extract information from images that may not be obvious to visual

* Corresponding author at: Biomedical Engineering Department, Washington University in St Louis, United States.
E-mail address: zhu.q@wustl.edu (Q. Zhu).

https://doi.org/10.1016/j.pacs.2024.100675
Received 15 September 2024; Received in revised form 31 October 2024; Accepted 27 November 2024
Available online 29 November 2024

perception. In this study, using in vivo ovarian lesion data acquired from 68 patients with 93 ovarian lesions [13], we computed quantitative US and PA parameters from RF data and extracted radiomic features from US and PAT images. We then developed a machine learning model based on an optimized subset of these features to classify common lesion types. Adding the quantitative imaging features extracted from co-registered US-PAT significantly improved the diagnostic performance of O-RADS. To the best of our knowledge, this study is the first one to explore the utility of quantitative US and PA parameters and radiomic features to accurately diagnose complex adnexal/ovarian lesions of a considerable patient population.

2. Methods

2.1. Co-registered US-PAT imaging system

Imaging was performed with the transvaginal US-PAT system described previously in [12,13]. In this system, PAT signals are excited by light from a tunable Ti:Sapphire pulsed laser (LOTIS TII, Minsk, Belarus) delivered to the tissue through four optical fibers, as shown in Fig. 1 [20]. Co-registered US and PAT scans are acquired with a commercial transvaginal US system (E-CUBE 12, Alpinion Medical Systems, Republic of Korea). PAT data was acquired at four wavelengths around the isosbestic point for oxy- and deoxyhemoglobin at 808 nm: 750, 780, 800, and 830 nm. Images at each wavelength were five-times averaged to improve the signal-to-noise ratio. The PAT images at the four wavelengths are acquired sequentially, interleaved with real-time US B mode imaging. Additionally, interleaved PAT and US beamforming allows for real-time co-registered US-PAT display during the imaging sessions.

2.2. Patient imaging

This study was approved by the Institutional Review Board of the Washington University School of Medicine. Between August 2020 and June 2022, 73 patients participated in the study. All patients provided informed consent. Each patient was first examined by a study radiologist using a clinical US system. The radiologist then imaged the patient with our US-PAT system and indicated the lesion's position on the B-scan US. A rectangular region of interest (ROI) was selected that contained either the entire lesion or the lesion's most significant features, such as papillary projections and internal solid components. Each lesion received two O-RADS scores, graded independently by two study radiologists. Among the 73 participating patients, five were excluded from data analysis because of either technical issues or the imaging limitations of our system. From the rest of the cohort, consisting of 68 patients, 93 ovaries or adnexal lesions were imaged and evaluated, as summarized in Table 1. All the patients included in this study were scheduled for oophorectomy after the imaging study, and the final pathological diagnoses after surgery were used as the ground truths in our analysis.

Table 1
Summary of all ovarian-adnexal lesions analyzed in this study: A total of 93 ovarian-adnexal lesions from a cohort of 68 patients. For some patients in the cohort, both ovaries were imaged and analyzed as separate samples.

Classification	Description
Cancer	Malignant ovarian/ adnexal lesion (n = 18)
	Borderline ovarian lesion (n = 1)
	Malignant tubal lesion (n = 2)
Benign	Cystic lesion (n = 23)
	Solid lesion (n = 12)
	Teratoma (n = 10)
	Endometriosis or adhesion (n = 14)
Normal	No abnormality identified by imaging or histopathology after surgical removal (n = 13)

2.3. Lesion characterization

Fig. 2 illustrates the procedure for characterizing and classifying an ovarian-adnexal lesion from a co-registered US-PAT scan. Each lesion is localized with a rectangular ROI, and its boundary is manually segmented. To describe the lesion's shape, a set of normalized shape features is computed from the lesion's contour. Then, within the ROI, parametric and radiomic features are computed from the co-registered US-PAT RF data and images, respectively. Using the extracted features, a classification model is trained to classify common lesion types and predict a lesion's malignancy risk.

2.3.1. Lesion shape features

To characterize the shape of an ovarian-adnexal lesion, we manually trace out its contour and compute three Zernike moments and 10 shape indices [21,22], as shown in Fig. 3. The three chosen Zernike moments reflect the contour's roundedness ($\varphi_{4,2}$), shape irregularity ($\varphi_{6,0}$), and boundary distinctness ($\varphi_{9,7}$) [21]. Similarly, the ten shape indices measure the shape's elongation (extension 1, extension 2), convexity (convexity 1, convexity 2), deviation from an oval shape (φ_{MA}, φ_R, φ_D), and boundary irregularity (N_{cc}, circularity, deficit). To ameliorate incomplete viewing of the lesion by US, all shape features are normalized.

2.3.2. US parametric features

To characterize a lesion's acoustic properties, four US parameters were extracted inside the ROI (Fig S1). First, Nakagami imaging (TSI) was implemented to reflect local acoustic scatterer concentrations [23]. Second, the local speed of sound (SoS) inside the tissue was estimated using a custom algorithm adapted from [24]. Third, the local acoustic

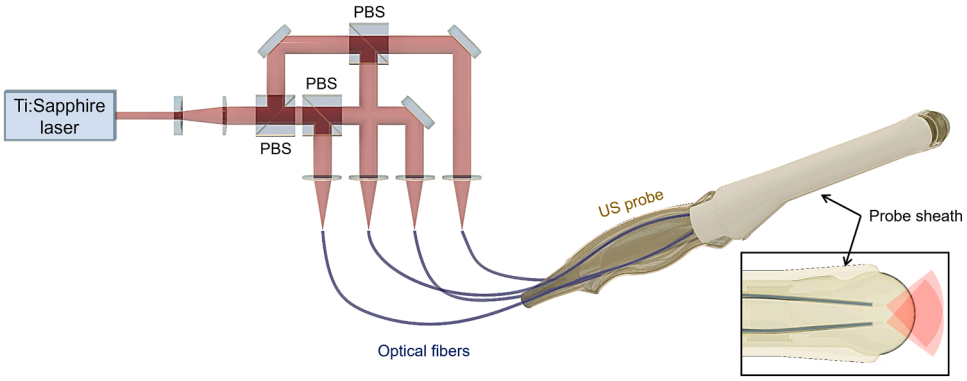

Fig. 1. Co-registered US-PAT system. Light from a tunable Ti:Sapphire pulsed laser is coupled evenly into four optical fibers through a compact optical setup involving three polarizing beam splitters (PBS). Two optical fibers deliver illumination from each side of the US probe. A thin resin sheath covers the US probe with the optical fibers and improves the illumination uniformity through the diffuse reflective coating on its inside surface.

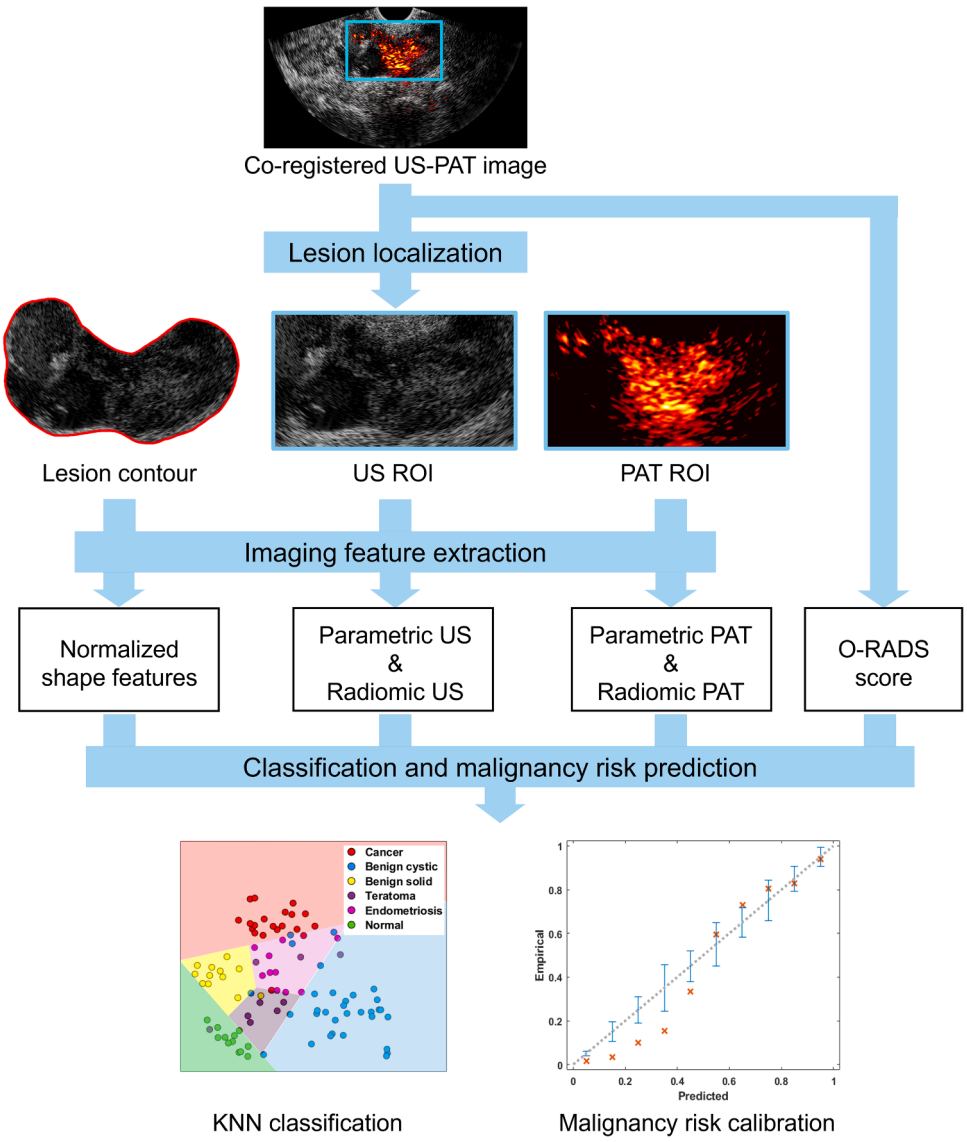

Fig. 2. Procedure for lesion characterization and classification from a co-registered US-PAT scan.

attenuation (TAI) was estimated by computing the local decrease rate of the US center frequency as a function of the imaging depth [25]. Finally, short-lag spatial-coherence (SLSC) imaging provided a source of nonlinear US contrast. SLSC is a coherence–based beamforming technique that has been shown to reduce clutter and enhance lesion definition in a nonlinear signal-dependent fashion [26,27]. For comparison between lesions, the mean and variance of each parameter inside the ROI were calculated.

2.3.3. US radiomic features

We computed 41 radiomic features characterizing a lesion's textural appearance on the US image. They included 14 based on the gray level co-occurrence matrix (GLCM) [28], 14 based on the neighborhood gray level dependence matrix (NGLDM) [29], and 13 based on the gray level size-zone matrix GLSZM [21]. Compared to parametric techniques, radiomics is more sensitive to intra-tumoral heterogeneity, especially to local and subtle variations (Fig S2). To ensure feature stability and reproducibility, all ROIs were normalized with respect to the brightest pixel in their corresponding US scan and discretized to 32 gray levels. All the radiomic statistics were normalized using Yeo-Johnson transform followed by z-transform.

2.3.4. PAT parametric features

Four PA parameters were extracted (Fig S3). First, using the data at all four wavelengths, the relative oxyhemoglobin concentration ($[HbO_2]$) and deoxyhemoglobin concentration ($[HbR]$) were estimated using linear spectral unmixing. Then, the relative total hemoglobin concentration (THb) was calculated as $THb = [HbO_2] + [HbR]$, and the level of oxygen saturation (sO_2) was calculated as $sO_2 = [HbO_2]/THb$. To reduce the impact of outliers and ROI size variations, the mean value of each lesion parameter was calculated as the weighted mean inside the full width at half-maximum of its distribution. In addition, linear regression was applied to the mid-band section of the PA power spectrum to compute the mid-band slope and intercept [30].

2.3.5. PAT radiomic features

We computed 41 radiomic features of the PAT ROI, using the same method as for the co-registered US ROI (Fig S4).

Finally, for each lesion the average of the O-RADS scores from two study radiologists was included. In total, we extracted 112 imaging features from each lesion, including 62 US features, 49 PA features, and one O-RADS score. Because multiple scans were collected from the same lesion, the average results were used to improve the feature stability.

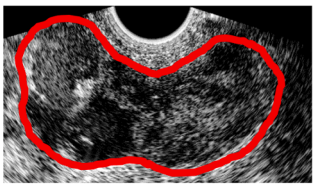

Geometric quantity	Shape feature	Illustration
$f(r,\theta)$	Zernike moments for $\varphi_{4,2}, \varphi_{6,0}, \varphi_{9,7}$ where $\varphi_{m,n}(f) = \int_{r=0}^{r_{max}} \int_{\theta=-\pi}^{\pi} Z_n^m(r,\theta) \cdot f(r,\theta) d\theta\, dr$	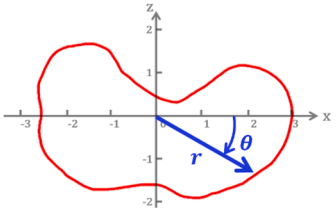
ρ_i, ρ_e	$extension1 = \rho_i/\rho_e$ $deficit = 1 - \frac{\pi(\rho_e - \rho_i)^2}{P^2}$	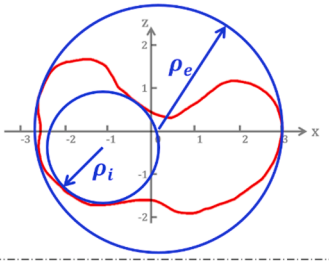
$C_H(f)$	$convexity1 = \frac{Area(f)}{Area(C_H(f))}$ $convexity2 = \frac{P(C_H(f))}{P(f)}$ $Ncc = \frac{1}{1 + Card(C_H(f) \backslash f)}$	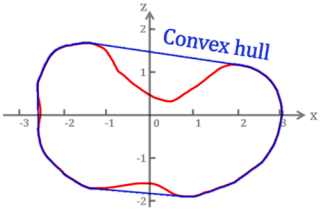
L_{SA}, L_{MA}	$\varphi_{MA} = \frac{\pi L_{SA} \times L_{MA}}{Area(f)}$	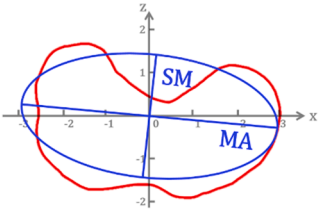
R_{min}, R_{max}	$circularity = R_{min}/R_{max}$ $\varphi_R = \frac{\pi R_{min} \times R_{max}}{Area(f)}$	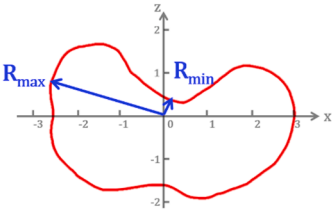
ED_F, D_F	$extension2 = ED_F/D_F$ $\varphi_D = \frac{\pi ED_F \times D_F}{Area(f)}$	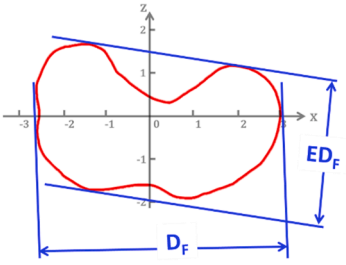

(caption on next page)

Fig. 3. Features describing the shape of an ovarian-adnexal lesion. The red line delineates the lesion's contour on the US B scan. The contour, f, is represented in a Cartesian coordinate system centered at the shape's center of mass (CM) in centimeters. Here, ρ_i and ρ_e are respectively the radii of the maximum inscribed circle and the minimum circumscribed circle. Further, $C_H(f)$ denotes the contour's convex hull, and MA and SA denote the semi-major and semi-minor axes of the best-fit ellipse for the contour. $R_{\max}$ and $R_{\min}$ are the maximum and minimum distances from the CM to f, and D_F and ED_F are the maximum and minimum Feret distances, respectively. *Card*() denotes the cardinality operator or the number of connected components, and $P()$ denotes the perimeter of a shape.

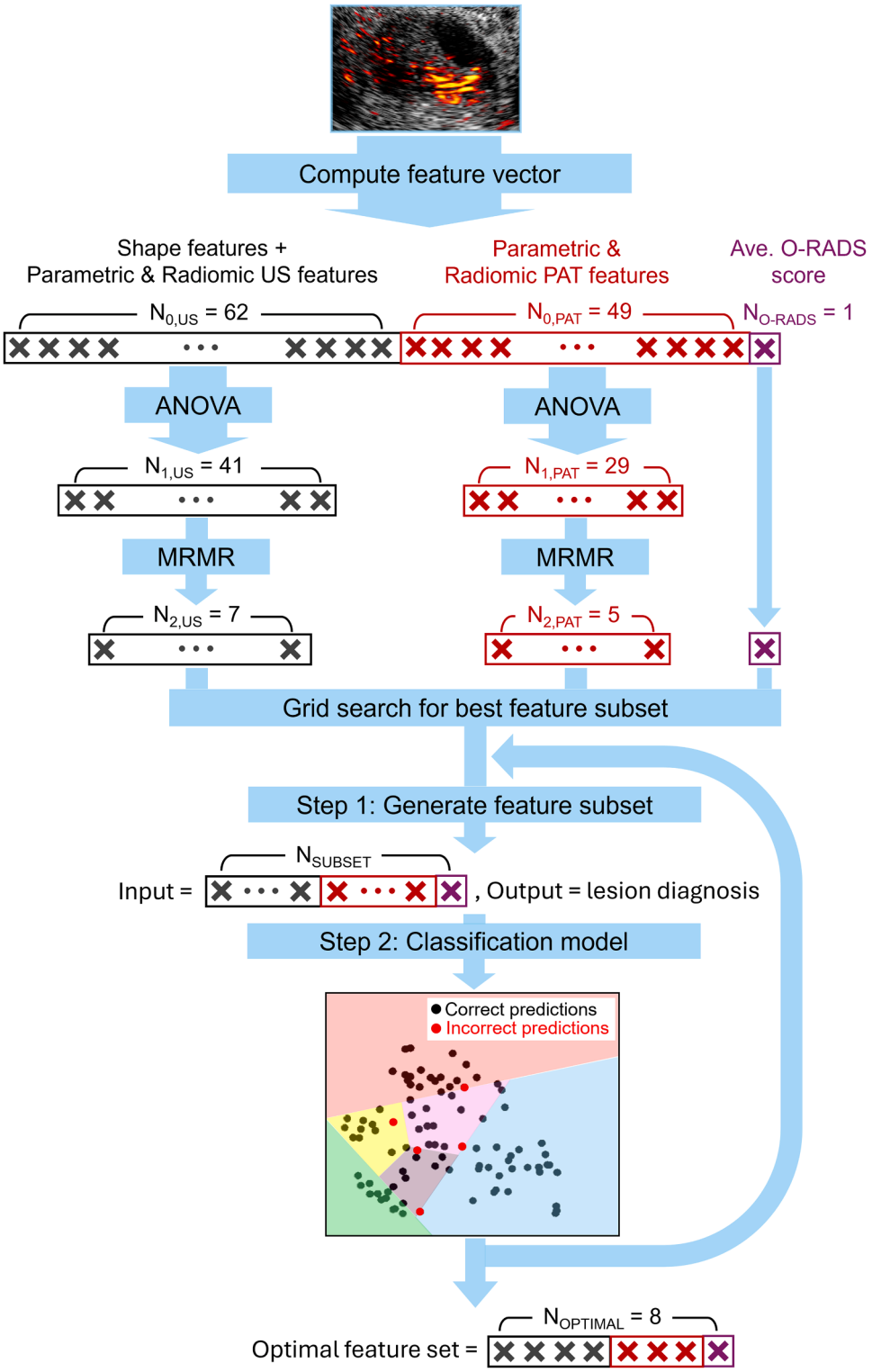

Fig. 4. Procedure for imaging feature selection. ANOVA: analysis of variance followed by Tukey-Kramer test. MRMR: maximum-relevance minimum-redundancy algorithm.

2.4. Lesion classification and statistical analysis

Using the extracted features, classification models were developed to differentiate six classes of ovarian-adnexal lesions: cancer, benign cystic lesions, benign solid lesions, teratoma, endometriosis, and normal ovaries.

To select significant US and PA features, each feature was first tested using one-way ANOVA. A feature was excluded if none of the pair-wise p-values calculated from the Tukey-Kramer test was less than 0.01. Because ANOVA favors features with low intraclass variance and high interclass variance while imposing relatively loose confidence limits, this initial test aimed to eliminate features that provide little to no discrimination between categories. Then, the minimum-redundancy maximum-relevance algorithm (MRMR) was employed to separately rank the remaining US and PA features. Unlike ANOVA, which assesses each feature independently, MRMR additionally reduces feature redundancy by minimizing correlations between selected features. Thus, MRMR was applied here as the secondary screening test to remove features that were either insignificant or redundant compared to some other better-performing features. Finally, seven US features and five PA features with the highest predictor importance scores, along with the O-RADS score, were used for model training during which an exhaustive grid search was performed to determine the optimal feature subset.

Each diagnostic category in the dataset was randomly split into a training set and a validation set in a 3:1 ratio. Each model was trained 10^3 times with different random train-validation splits to assess its diagnostic performance and stability. An exhaustive search determined the best subset of features based on four criteria: (1) classification accuracy, (2) PPV, (3) fluctuation between different train-validation splits, and (4) cancer-vs-rest AUC, where the rest contains all benign lesion types and normal ovaries. The first three criteria were weighted so that the numbers of cancer and benign cases were balanced (Fig S5). The KNN model structure was selected because it produced the best diagnostic performance compared to other classification models (Table S1).

The optimized model was a KNN model with eight features, including four US features (shape convexity, mean SLSC, GLCM ASM, and GLCM IDM), three PA features (mean THb, mean sO2, and GLCM SVAR), and the average O-RADS score. The procedure for imaging feature selection is summarized in Fig. 4.

To better understand the significance of the selected features, a relative measure of feature importance was computed. Feature importance heavily depends on the classification model [31,32]. Therefore, more objective feature importance was obtained by averaging the importance values calculated by four methods: the permutation feature importance of a linear multinomial regression model and a nonlinear KNN model, the out-of-bag feature importance of a random forest model, and the feature importance from the ReliefF algorithm. Additionally, the local feature importance for cancer-versus-rest classification was computed using a similar method.

Further, the model was calibrated with the reliability curve to predict a realistic malignancy risk matching the empirical probability of malignancy (Fig S6).

3. Results

Fig. 5 shows representative US-PAT images of different ovarian lesions. Fig. 6 shows the statistical distributions of six features that were significant in differentiating various ovarian pathologies. All malignant lesions received O-RADS scores ≥ 4, and all normal ovaries were correctly scored as 1 (Fig. 6**a**). However, the O-RADS scores showed high uncertainty in assessing benign lesions, suggesting high sensitivity but inadequate specificity. Comparison of the lesion convexity showed that while normal ovaries appeared oval with convexities close to 1, benign cystic or solid lesions were less convex, and cancer and teratoma had still more irregular shapes (Fig. 6**b**). SLSC is a measure of the local spatial coherence of US signals. Fig. 6**c** suggests that most cancers had low SLSC due to their complex and heterogeneous composition, whereas benign solid lesions had the highest SLSC. IDM is a radiomic feature describing the local homogeneity of US signal intensities. Cystic lesions had the highest IDM because they were fluid-filled and uniformly hypo-echoic in US. In contrast, solid lesions had the lowest IDM, due to hyper-echoic fibrotic tissue that generated significant US speckles (Fig. 6**f**). Functional markers of different lesions were extracted from co-registered PAT. Fig. 5 shows that cancer and endometriosis had stronger and more diffusely distributed PA signals than benign lesions, matching the quantitative comparison of THb concentrations shown in Fig. 6**e**: the THb of endometriosis was elevated compared to that of other benign lesions, while cancer had significantly higher THb than all benign pathologies. Fig. 6**d** shows that the sO2 level of endometriosis was comparable to that of other benign pathologies, but cancer had lower sO2 than all benign lesions. Therefore, while endometriosis and cancer had similar presentations on single-wavelength PAT, they could be separated

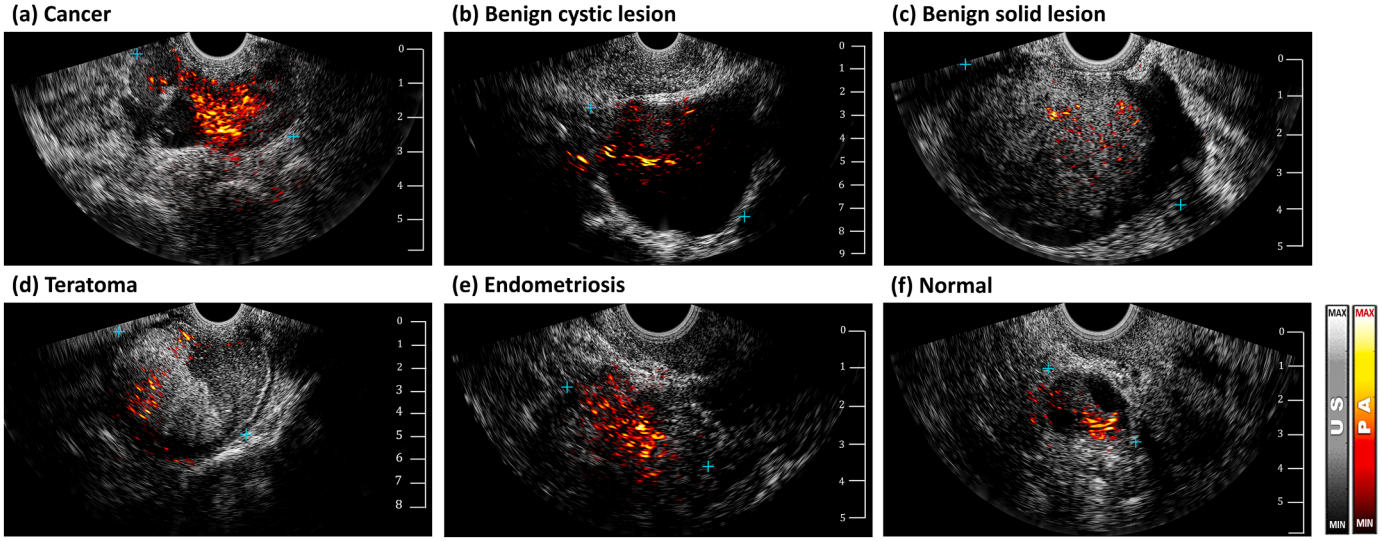

Fig. 5. Example co-registered US-PAT B scans of different ovarian-adnexal lesions. PAT images in hot color maps are overlaid on co-registered grayscale US images. The top left and bottom right corners of the ovarian-adnexal lesion or the normal ovary are marked by blue '+ ' symbols on each scan. The images are displayed with the same dynamic range: 60 dB for US images and 35 dB for PAT images.

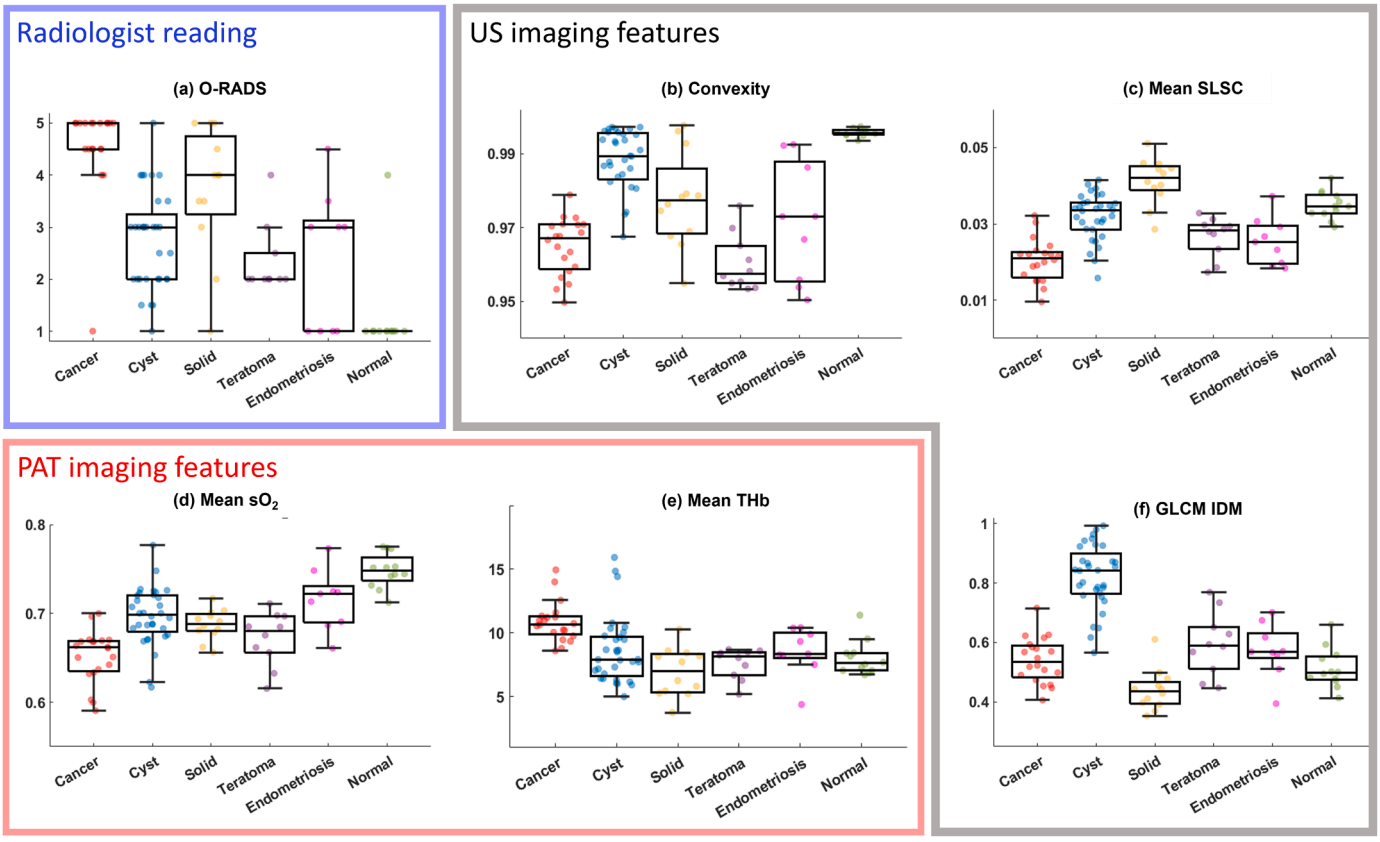

Fig. 6. Distributions of six example imaging features that were significant in differentiating different ovarian-adnexal pathologies.

using the combination of THb and sO2.

Fig. 7**a** shows that for differentiating cancer from benign lesions, adding either PAT or US features to the O-RADS score significantly improved the model's AUC. The KNN model based only on O-RADS scores had an AUC of 0.871 (95 % CI: 0.853–0.889). In comparison, with both the PAT and US features, the model's AUC was improved to 0.969 (95 %CI: 0.961–0.977). The PAT features predominantly improved the model's sensitivity, whereas the US features mainly improved its specificity, resulting in a leftward shift of the ROC curve. This observation implied that an elevated THb and decreased sO2 caused the model to predict a higher malignancy risk when a lesion's O-RADS score was < 5, whereas the US features were important in downgrading benign lesions with O-RADS scores ≥ 4. Fig. 7**b** suggests that a high THb, high O-RADS score and low US SLSC were the most critical markers of malignancy.

Fig. 8**a** summarizes the six-class classification performance of the US-PAT KNN model compared to the models with fewer imaging features. Incorporating either PAT or US features allowed for more nuanced lesion classification. When all imaging features were considered, the model achieved a balanced classification accuracy of 86.0 ± 0.8 %. When calculating the balanced classification accuracy, the cancer accuracy was weighted to match the total number of benign categories. Fig. 8**b** shows the comparative importance of the features to the model's global performance, where each category is weighted equally. The importance of the three radiomic features is significantly elevated, suggesting their ability to differentiate benign pathologies with subtler differences.

Table 2 demonstrates the model's performance when applied to three lesions unused during model training. Table 2**a** shows an ovary

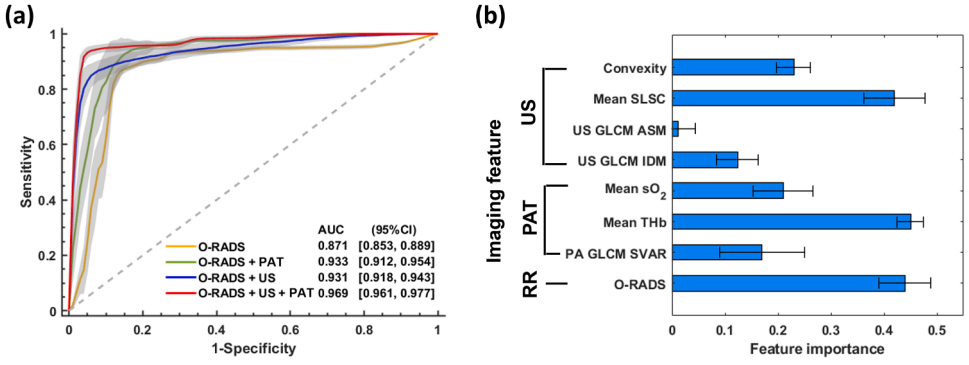

Fig. 7. (a) Average ROC curves of KNN models for differentiating cancer from benign lesions and normal ovaries. The diagnostic performance of the KNN model using the O-RADS score as its only predicting variable was compared to that of the models including quantitative PAT and/or US imaging features. The gray shaded areas show the standard deviation of each ROC curve. The average and the 95 % confidence interval of the AUC for each ROC is marked in the legend. (b) The relative importance of the imaging features contributing to cancer prediction. RR: radiologist reading.

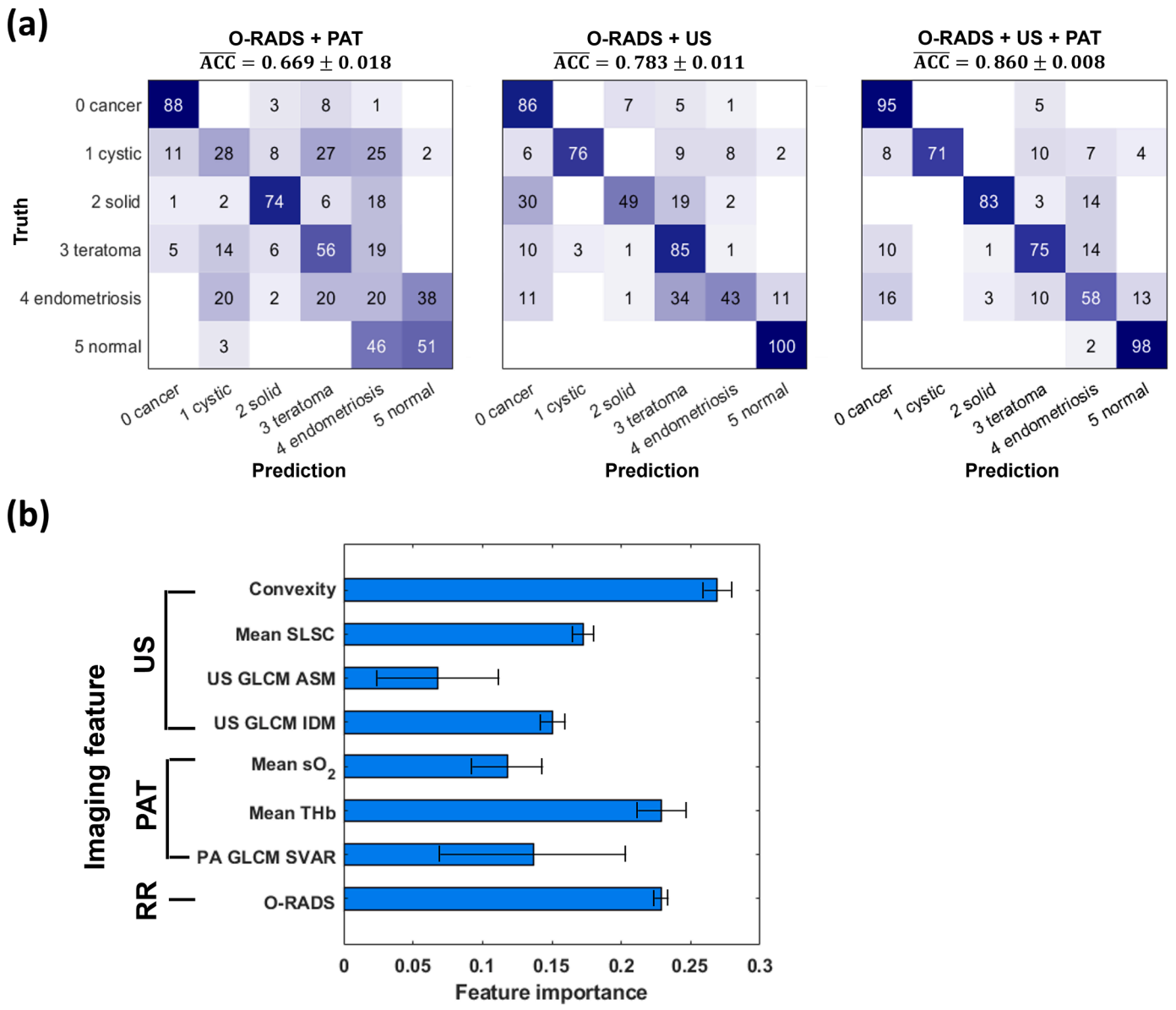

Fig. 8. (a) Global model performance for six-class classification, with and without the addition of quantitative PAT and/or US imaging features. The numbers in the confusion matrices are shown in percentages normalized by the case numbers in each category. $\overline{ACC}$ = balanced classification accuracy. (b) Relative feature importance to the unweighted classification task. RR: radiologist reading.

with high grade serous carcinoma. The US-PAT image showed a complex solid lesion with diffuse internal vasculature. The US-PAT KNN model correctly predicted cancer with a malignancy risk of 0.753, consistent with the O-RADS assessment. Table 2**b** shows a large benign fibroma that appeared hyper-echoic with shadowing on US, and showed sparse vascularity on PA. The study radiologists gave an O-RADS score of 5, referring the patient to further consultation. The US-PAT KNN model correctly classified the lesion as a benign solid lesion with a malignancy risk of 0.313, downgrading it from its initial O-RADS assessment. Table 2**c** shows a benign lesion with endometriosis and stromal calcification. The study radiologists gave an average O-RADS score of 4.5 because the lesion had multiple papillary projections and showed high vascularity in Doppler US. Despite relatively high ambiguities in the prediction scores, the model correctly classified the lesion with a malignancy risk of 0.231, correctly downgrading the lesion from its O-RADS assessment.

4. Discussion

In our previous work, we found that co-registered PAT hemoglobin concentration and oxygen saturation helped improve the diagnostic accuracy in assessing a lesion's malignancy risk using O-RADs [13]. Here, we have advanced from binary malignant-vs-benign differentiation to more nuanced classifications. A set of US-PAT imaging features was created by combining parametric features from co-registered RF data and radiomic features from co-registered US-PAT images. We selected an optimal subset of eight US and PAT imaging features that provided the best performance in differentiating various ovarian-adnexal pathologies. Comparing the significance of PAT and US features, we observed that PAT features improved the model's confidence in cancer diagnosis when a lesion showed heightened vascularity and lowered oxygen saturation. However, different benign pathologies could not be effectively separated with PAT features alone. US features mainly improved the model's specificity and differentiation between benign pathologies. Additionally, we found that parametric features

Table 2
Representative test images unused during model training, and their calibrated malignancy risk predicted by the US-PAT KNN model. The top left and bottom right corners of the lesion are marked with blue '+ ' symbols on each scan. In (c), the stromal calcification is indicated by the pink arrow. In the plots for model prediction scores, the six numbered categories are C = cancer, BC = benign cystic, BS = benign solid, T = teratoma, E = endometriosis, N = normal.

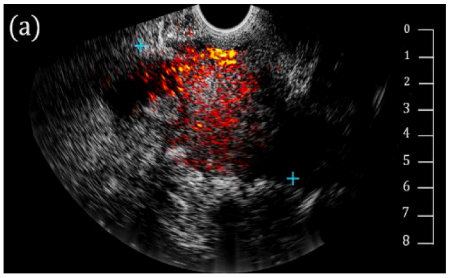	High grade serous carcinoma	5 High risk (≥50%)	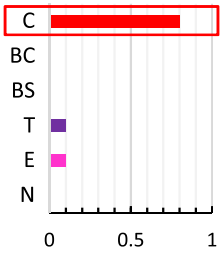	0.753
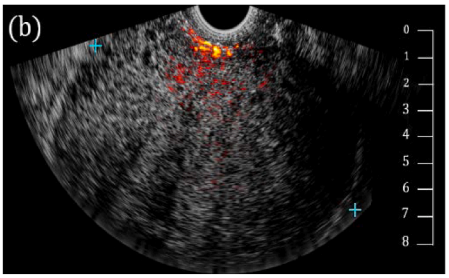	Fibroma	5 High risk (≥50%)	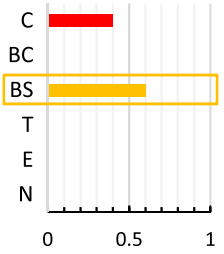	0.313
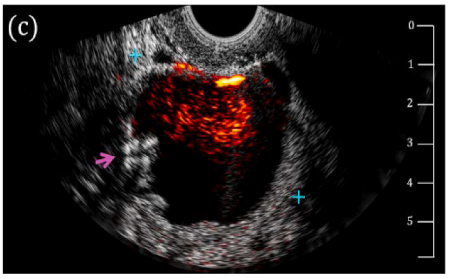	Endometriosis with stromal calcification	4.5 Intermediate (10-50%) to high risk (≥50%)	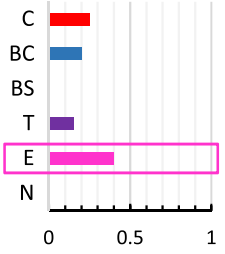	0.231

were more significant for predicting malignancy, whereas radiomic features helped the model better differentiate between benign pathologies. Interestingly, whereas many US radiomic features demonstrated differentiating capability for different pathologies to some extent, only one PAT radiomic feature showed sufficient significance compared to parametric PAT features. The reason was that B-scan PAT, as a functional imaging technique, does not provide as much morphological information as US, while high-resolution morphological details are critical for radiomics to provide stable and accurate results [33].

To generalize the model and potentially facilitate the radiologists' assessment of various lesions, we calibrated the model to predict a malignancy risk in a graded manner similar to the O-RADS system. The calibrated malignancy risks were validated on three cases unused during model training, including one cancer, one fibroma, and one endometriosis. The model predicted reasonable malignancy risks for all three testing cases, downgrading both benign cases with high O-RADS scores. Although endometriosis is a prevalent benign disease, it is difficult to diagnose through imaging because of its complex phenotypes and the lack of a specific biomarker [34]. We found that endometriosis had a heterogeneous appearance in US images and an elevated vascularity that mimics cancer. Among other lesion categories, the US-PAT KNN model exhibited lowest sensitivity and PPV in identifying endometriosis (Fig. 6**a**). This finding agrees with radiologists' clinical experience because endometriosis is indeed often misdiagnosed as other diseases. Nevertheless, the US-PAT KNN model predicted moderate to low malignancy risk for endometriosis, suggesting that the imaging features effectively downgraded endometriosis that has high O-RADS scores. It should be noted that due to the limited sample size, the model's generalizability was tested through cross-validation. As more patient data are being collected, this model will be conducted on an independent test set. More generally, we demonstrated that analyzing US and PAT images with physics-based parametric and statistics-based radiomic algorithms allowed us to extract richer, more nuanced features, enhancing classification accuracy beyond conventional subjective diagnostic criteria. Therefore, our proposed method can also serve as the backbone of a more comprehensive analysis pipeline for US and PAT image data and be extended to other diagnostic or treatment monitoring applications [35–38].

Because ovarian-adnexal lesions constitute a wide range of heterogeneous pathologies, simplistic malignant-vs-benign classification is not sufficient. Additionally, there is significant variation in the lesion presentation even within the same subcategory. As a result, the size of the study population is a main limitation, and the model's generalizability could be affected because the model did not include some rarer pathologies during training. We mitigated this limitation by selecting a simple model architecture and the smallest subset of imaging features. Feature space dimensionality can be reduced through either feature selection or feature fusion. Here, we focused on the former technique for the interpretability of the final feature set. We note that it is possible to further enhance the model performance with feature fusion methods

including Principal Component Analysis (PCA) and Singular Value Decomposition (SVD) for linear fusion, and t-distributed stochastic neighbor embedding (t-SNE) and Uniform Manifold Approximation and Projection (UMAP) nonlinear fusion [39]. However, as these methods would reduce interpretability, they were not used in this study. As more data from a wider variety of pathologies are being collected, we will obtain a more comprehensive representation of each lesion subcategory. Additionally, more sophisticated model architectures [40] could be adopted to further improve the diagnostic performance. A more nuanced classification of lesions than provided by the current O-RADS system is also of great clinical value because more targeted clinical management requires not only recognizing when a lesion is benign, but also accurately diagnosing its type. This is especially true for smaller lesions, where surgery may be unnecessary depending on the lesion's pathology.

To be deployed in a clinical setting, the analytical procedure will be automated. The manual lesion segmentation can be replaced by a deep learning method for segmenting lesions on US images [41]. Diseased vasculature manifests in changes in both vascularity and vascular morphology. An ongoing effort to extract more morphological information from PAT seeks to improve the image resolution and create multi-perspective 3D reconstruction using deep learning [42].

CRediT authorship contribution statement

Quing Zhu: Writing – review & editing, Supervision, Project administration, Methodology, Investigation, Funding acquisition, Data curation, Conceptualization. **Yixiao Lin:** Writing – review & editing, Writing – original draft, Validation, Software, Methodology, Investigation, Formal analysis, Data curation, Conceptualization.

Declaration of Competing Interest

The authors declare that they have no known competing financial interests or personal relationships that could have appeared to influence the work reported in this paper

Acknowledgments

The study is supported by the National Institutes of Health (R01CA237664). We thank the abdominal radiologists of the Radiology Department of the School of Medicine, Washington University in St Louis, for helping with the US imaging of the patients. We also thank the gynecologic surgeons of the Department of Obstetrics & Gynecology, School of Medicine, Washington University in St Louis, for helping with recruiting patients.

Appendix A. Supporting information

Supplementary data associated with this article can be found in the online version at doi:10.1016/j.pacs.2024.100675.

Data Availability

Data will be made available on request.

References

[1] R.F. Andreotti, D. Timmerman, L.M. Strachowski, W. Froyman, B.R. Benacerraf, G. L. Bennett, P. Glanc, O-RADS US risk stratification and management system: a consensus guideline from the ACR ovarian-adnexal reporting and data system committee, Radiology 294 (1) (2020) 168–185.
[2] L.M. Strachowski, P. Jha, C.H. Phillips, M.M. Blanchette Porter, W. Froyman, P. Glanc, R.F. Andreotti, O-RADS US v2022: an update from the American College of Radiology's Ovarian-Adnexal Reporting and Data System US Committee, Radiology 308 (3) (2023) e230685.
[3] P. Jha, A. Gupta, T.M. Baran, K.E. Maturen, K. Patel-Lippmann, H.M. Zafar, E. A. Sadowski, Diagnostic performance of the Ovarian-Adnexal Reporting and Data System (O-RADS) ultrasound risk score in women in the United States, JAMA Netw. Open 5 (6) (2022) e2216370-e2216370.
[4] E.A. Sadowski, I. Thomassin-Naggara, A. Rockall, K.E. Maturen, R. Forstner, P. Jha, C. Reinhold, O-RADS MRI risk stratification system: guide for assessing adnexal lesions from the ACR O-RADS committee, Radiology 303 (1) (2022) 35–47.
[5] I. Thomassin-Naggara, E. Poncelet, A. Jalaguier-Coudray, A. Guerra, L.S. Fournier, S. Stojanovic, A.G. Rockall, Ovarian-adnexal reporting data system magnetic resonance imaging (O-RADS MRI) score for risk stratification of sonographically indeterminate adnexal masses, JAMA Netw. Open 3 (1) (2020) e1919896-e1919896.
[6] J. Xu, Z. Huang, J. Zeng, Z. Zheng, J. Cao, M. Su, X. Zhang, Value of contrast-enhanced ultrasound parameters in the evaluation of adnexal masses with ovarian–adnexal reporting and data system ultrasound. Ultrasound Med. Biol. 49 (7) (2023) 1527–1534.
[7] K. Yuan, Y.J. Huang, M.Y. Mao, T. Li, S.J. Wang, D.N. He, Y.X. Zhu, Contrast-enhanced US to improve diagnostic performance of O-RADS US risk stratification system for malignancy, Radiology 308 (2) (2023) e223003.
[8] M. Ishihara, A. Horiguchi, H. Shinmoto, H. Tsuda, K. Irisawa, T. Wada, T. Asano, Comparison of transrectal photoacoustic, Doppler, and magnetic resonance imaging for prostate cancer detection (March), in: Photons Plus Ultrasound: Imaging and Sensing 2016, 9708, SPIE, 2016, pp. 894–899 (March).
[9] S. Hu, L.V. Wang, Photoacoustic imaging and characterization of the microvasculature, J. Biomed. Opt. 15 (1) (2010), 011101-011101.
[10] W. Choi, E.Y. Park, S. Jeon, C. Kim, Clinical photoacoustic imaging platforms, Biomed. Eng. Lett. 8 (2018) 139–155.
[11] A.A. Oraevsky, B. Clingman, J. Zalev, A.T. Stavros, W.T. Yang, J.R. Parikh, Clinical optoacoustic imaging combined with ultrasound for coregistered functional and anatomical mapping of breast tumors, Photoacoustics 12 (2018) 30–45.
[12] S. Nandy, A. Mostafa, I.S. Hagemann, M.A. Powell, E. Amidi, K. Robinson, Q. Zhu, Evaluation of ovarian cancer: initial application of coregistered photoacoustic tomography and US, Radiology 289 (3) (2018) 740–747.
[13] Q. Zhu, H. Luo, W.D. Middleton, M. Itani, I.S. Hagemann, A.R. Hagemann, C. L. Siegel, Characterization of adnexal lesions using photoacoustic imaging to improve sonographic O-RADS risk assessment. Ultrasound Obstet. Gynecol. 62 (6) (2023) 891–903.
[14] J. Mamou, M.L. Oelze (Eds.), Quantitative Ultrasound in Soft Tissues, Springer Netherlands, Dordrecht, 2013, pp. 1–25.
[15] M.L. Oelze, J. Mamou, Review of quantitative ultrasound: Envelope statistics and backscatter coefficient imaging and contributions to diagnostic ultrasound, IEEE Trans. Ultrason., Ferroelectr., Freq. Control 63 (2) (2016) 336–351.
[16] A.M. Pirmoazen, A. Khurana, A. El Kaffas, A. Kamaya, Quantitative ultrasound approaches for diagnosis and monitoring hepatic steatosis in nonalcoholic fatty liver disease, Theranostics 10 (9) (2020) 4277.
[17] J.E. Van Timmeren, D. Cester, S. Tanadini-Lang, H. Alkadhi, B. Baessler, Radiomics in medical imaging — "how-to" guide and critical reflection, Insights into Imaging 11 (1) (2020) 1–16.
[18] P. Lambin, R.T. Leijenaar, T.M. Deist, J. Peerlings, E.E. De Jong, J. Van Timmeren, S. Walsh, Radiomics: the bridge between medical imaging and personalized medicine, Nat. Rev. Clin. Oncol. 14 (12) (2017) 749–762.
[19] H.T. Hu, Z. Wang, X.W. Huang, S.L. Chen, X. Zheng, S.M. Ruan, M. Kuang, Ultrasound-based radiomics score: a potential biomarker for the prediction of microvascular invasion in hepatocellular carcinoma, Eur. Radiol. 29 (2019) 2890–2901.
[20] Y. Lin, S. Kou, Y. Zou, K. Maslov, Q. Zhu, Cylindrical lens configuration for optimizing light delivery in a curvilinear endocavity photoacoustic imaging system, Opt. Lett. 48 (9) (2023) 2417–2420.
[21] G. Thibault, B. Fertil, C. Navarro, S. Pereira, P. Cau, Levy, J.L. Mari, Shape and texture indexes application to cell nuclei classification, Int. J. Pattern Recognit. Artif. Intell. 27 (1) (2013) 1357002.
[22] F. Saki, A. Tahmasbi, H. Soltanian-Zadeh, S.B. Shokouhi, Fast opposite weight learning rules with application in breast cancer diagnosis, Comput. Biol. Med. 43 (1) (2013) 32–41.
[23] P.H. Tsui, C.C. Chang, Imaging local scatterer concentrations by the Nakagami statistical model, Ultrasound Med. Biol. 33 (4) (2007) 608–619.
[24] M. Jakovljevic, S. Hsieh, R. Ali, G. Chau Loo Kung, D. Hyun, J.J. Dahl, Local speed of sound estimation in tissue using pulse-echo ultrasound: model-based approach, J. Acoust. Soc. Am. 144 (1) (2018) 254–266.
[25] H. Kim, T. Varghese, Attenuation estimation using spectral cross-correlation, ieee Trans. Ultrason., Ferroelectr., Freq. Control 54 (3) (2007) 510–519.
[26] M.A. Lediju, G.E. Trahey, B.C. Byram, J.J. Dahl, Short-lag spatial coherence of backscattered echoes: imaging characteristics, IEEE Trans. Ultrason., Ferroelectr., Freq. Control 58 (7) (2011) 1377–1388.
[27] J.J. Dahl, D. Hyun, M. Lediju, G.E. Trahey, Lesion detectability in diagnostic ultrasound with short-lag spatial coherence imaging, Ultrason. Imaging 33 (2) (2011) 119–133.
[28] R.M. Haralick, K. Shanmugan, I. Dinstein, Textural features for image classification, *IEEE Trans. Syst., Man, Cyber*, SMC 3 (1973) 610–621.
[29] C. Sun, W.G. Wee, Neighboring gray level dependence matrix for texture classification, Comput. Vis., Graph., Image Process. 23 (3) (1983) 341–352.
[30] R.E. Kumon, C.X. Deng, X. Wang, Frequency-domain analysis of photoacoustic imaging data from prostate adenocarcinoma tumors in a murine model, Ultrasound Med. Biol. 37 (5) (2011) 834–839.
[31] M. Saarela, S. Jauhiainen, Comparison of feature importance measures as explanations for classification models, SN Appl. Sci. 3 (2021) 1–12.

[32] D. Rengasamy, B.C. Rothwell, G.P. Figueredo, Towards a more reliable interpretation of machine learning outputs for safety-critical systems using feature importance fusion, Appl. Sci. 11 (24) (2021) 11854.
[33] A. Traverso, L. Wee, A. Dekker, R. Gillies, Repeatability and reproducibility of radiomic features: a systematic review, Int. J. Radiat. Oncol. Biol. Phys. 102 (4) (2018) 1143–1158.
[34] J. Quesada, K. Härmä, S. Reid, T. Rao, G. Lo, N. Yang, N. Borok, Endometriosis: a multimodal imaging review, Eur. J. Radiol. 158 (2023) 110610.
[35] S.C. Hester, M. Kuriakose, C.D. Nguyen, S. Mallidi, Role of ultrasound and photoacoustic imaging in photodynamic therapy for cancer, Photochem. Photobiol. 96 (2) (2020) 260–279.
[36] Z. Wu, F. Duan, J. Zhang, S. Li, H. Ma, L. Nie, In vivo dual-scale photoacoustic surveillance and assessment of burn healing, Biomed. Opt. Express 10 (7) (2019) 3425–3433.
[37] Q. Li, K. Chen, W. Huang, H. Ma, X. Zhao, J. Zhang, L. Nie, Minimally invasive photothermal ablation assisted by laparoscopy as an effective preoperative neoadjuvant treatment for orthotopic hepatocellular carcinoma, Cancer Lett. 496 (2021) 169–178.
[38] E.I. Neuschler, R. Butler, C.A. Young, L.D. Barke, M.L. Bertrand, M. Böhm-Vélez, B. E. Dogan, A pivotal study of optoacoustic imaging to diagnose benign and malignant breast masses: a new evaluation tool for radiologists, Radiology 287 (2) (2018) 398–412.
[39] V.D. Calhoun, T. Adali, Feature-based fusion of medical imaging data, IEEE Trans. Inf. Technol. Biomed. 13 (5) (2008) 711–720.
[40] M.A. Azam, K.B. Khan, S. Salahuddin, E. Rehman, S.A. Khan, M.A. Khan, A. H. Gandomi, A review on multimodal medical image fusion: compendious analysis of medical modalities, multimodal databases, fusion techniques and quality metrics, Comput. Biol. Med. 144 (2022) 105253.
[41] Wang, Z. (2020). Deep learning in medical ultrasound image segmentation: a review. *arXiv preprint arXiv:2002.07703*.
[42] Y. Zou, Y. Lin, Q. Zhu, PA-NeRF, a neural radiance field model for 3D photoacoustic tomography reconstruction from limited Bscan data, Biomed. Opt. Express 15 (3) (2024).

Yixiao Lin is a Ph.D. student in biomedical engineering at Washington University in St. Louis. He received his bachelor's degree in biomedical engineering in 2020 from Washington University in St. Louis. His research focuses on technology development and clinical translation of ultrasound and photoacoustic imaging for cancer diagnosis.

Quing Zhu is the Edwin H. Murty Professor of Biomedical Engineering, at Washington University in St. Louis. She is also an associate faculty in Radiology, at the School of Medicine of Washington University in St. Louis. Professor Zhu has been named a Fellow of OSA, a Fellow of SPIE, and a Fellow of AIMBE. Her research interests include multi-modality ultrasound, diffuse light, photoacoustic imaging, and Optical Coherence Tomography for breast, ovarian, and colorectal cancer applications. She is interested in the development and applications of multi-modality machine learning models for cancer diagnosis and treatment prediction.